

A Green's function method for simulation of time-dependent solute transport and reaction in realistic microvascular geometries

TIMOTHY W. SECOMB*

Department of Physiology, University of Arizona, Tucson, AZ 85724-5051, USA

*Corresponding author: secomb@u.arizona.edu

[Received on 24 April 2015; revised on 24 August 2015; accepted on 3 September 2015]

A novel theoretical method is presented for simulating the spatially resolved convective and diffusive transport of reacting solutes between microvascular networks and the surrounding tissues. The method allows for efficient computational solution of problems involving convection and non-linear binding of solutes in blood flowing through microvascular networks with realistic 3D geometries, coupled with transvascular exchange and diffusion and reaction in the surrounding tissue space. The method is based on a Green's function approach, in which the solute concentration distribution in the tissue is expressed as a sum of fields generated by time-varying distributions of discrete sources and sinks. As an example of the application of the method, the washout of an inert diffusible tracer substance from a tissue region perfused by a network of microvessels is simulated, showing its dependence on the solute's transvascular permeability and tissue diffusivity. Exponential decay of the washout concentration is predicted, with rate constants that are about 10–30% lower than the rate constants for a tissue cylinder model with the same vessel length, vessel surface area and blood flow rate per tissue volume.

Keywords: solute transport; diffusion; permeability; microvessels; mathematical models; solute washout.

1. Introduction

Transport of solutes in the body occurs largely by convection along blood vessels and diffusion between blood vessels and surrounding tissues. Diffusive transport of a solute depends on its coefficient of molecular diffusivity, which is $\sim 10^{-5}$ cm²/s for very small solutes and decreases with increasing solute molecular weight. The diffusivity of a solute has important consequences for its spatial distribution. If the solute undergoes chemical reaction in the tissue, then spatial gradients must be present to maintain the supply to the tissue under steady-state conditions. For a given reaction rate, these spatial gradients are inversely proportional to the diffusivity. If the concentrations in the blood or the reaction rates in the tissue are time varying, the variation with time of concentrations in the tissue depends on the diffusivity.

In many cases of interest, the gradients in tissue are very steep. In the case of oxygen, for example, the maximum diffusion distance into oxygen-consuming tissue is in the range 20–100 μ m under typical physiological conditions (Secomb *et al.*, 1993), comparable with capillary spacing observed in the microcirculation. Substantial gradients in oxygen availability can therefore occur on the microvascular scale. Such gradients affect levels of other metabolites (Beard, 2006). Delivery of therapeutic drugs to tissue is restricted by diffusion in many cases. This problem is particularly significant for cancer drugs, because the vascular system of tumours is frequently disorganized, leading to inefficient perfusion and increased diffusion distances (Jain, 2005). The effectiveness of such drugs may be strongly influenced by their transport properties (Hicks *et al.*, 2006).

A number of theoretical approaches have been developed to simulate spatially distributed solute transport in the microcirculation. The Krogh cylinder model for oxygen transport, in which capillaries

are assumed to be arranged in a regularly spaced parallel array, has been widely used (Krogh, 1919; Middleman, 1972; Popel, 1989), but some features of solute transport in the microcirculation are not adequately described by models based on this model. Therefore, numerical techniques have been developed to simulate transport in more realistic and complex vascular geometries (Popel, 1989; Secomb *et al.*, 2004). One approach is to use finite-difference methods (Goldman and Popel, 2000, 2001; Beard and Bassingthwaite, 2001; Beard *et al.*, 2003; Lo *et al.*, 2003). This approach is relatively direct, and features such as time dependence and non-linearity in uptake or production rates are readily incorporated. The disadvantage is that fine meshes are required to give adequate resolution of a network of narrow vessels embedded in a tissue region, leading to a large number of unknowns and heavy computational demands. An alternative approach is to represent each vessel as a distribution of solute sources, so that the tissue solute concentration field is represented as a superposition of the fields resulting from these sources (Secomb and Hsu, 1988; Hsu and Secomb, 1989; Groebe, 1990; Hoofd *et al.*, 1990; Hoofd, 1992). This ‘Green’s function’ approach is more complex mathematically but requires fewer unknowns, leading to computational efficiency. Initially developed for steady-state problems with constant solute uptake (Hsu and Secomb, 1989), it was extended to cases with non-linear uptake kinetics (Secomb *et al.*, 1993).

The assumption of steady-state or quasi-steady-state conditions limits the applicability of the previously developed Green’s function method. In many cases of interest, the timescale for imposed changes in solute levels, resulting, for example, from sudden changes in metabolic demand or from infusion of drugs or tracers into the blood stream, may be seconds or minutes. The equilibration time for the diffusive distribution of solutes is of order L^2/D , where L is the diffusion distance and D is the diffusivity. For a typical diffusion distance of $100\text{ }\mu\text{m}$ and a typical small solute diffusivity of $10^{-5}\text{ cm}^2/\text{s}$, the diffusion time is $\sim 10\text{ s}$, and it increases for less diffusible solutes. If this time scale is not much shorter than the time scale for imposed changes in solute levels or reaction rates, then the assumption of quasi-steady diffusion may lead to significant errors.

The goal of the present work is to develop an efficient numerical method for simulating time-dependent reaction–diffusion–convection processes in realistic microvascular geometries. Conventional finite-difference methods are well developed for time-dependent diffusion and represent a logical approach. In many cases of interest, however, steep spatial gradients in solute concentration occur near microvessels, which necessitate a spatial step Δx no larger than a capillary diameter, typically about $5\text{ }\mu\text{m}$. To ensure accuracy and stability of the solution, the time step in a finite-difference analysis is restricted to $\Delta t \leq (\Delta x)^2/2D$, or 12.5 ms for $D = 10^{-5}\text{ cm}^2/\text{s}$. The representation of convective transport in microvessels also leads to a restriction on the time step, $\Delta t \leq \Delta x/u$ or about 5 ms for a typical velocity $u = 1\text{ mm/s}$. These limitations on Δt and Δx restrict the domain size and time interval for which conventional finite-difference methods are feasible.

The numerical approach presented here is designed to overcome these limitations. It places no restriction on the time step, provided that Δt is small enough to resolve the time-dependent processes of interest. Diffusive transport of solute is computed by convoluting the previous solute distribution with the solution of the diffusion equation for the spread of an instantaneous point source over the given time step (the time-dependent Green’s function). Convective transport is simulated by explicitly computing the displacement of fluid elements through the vessel network during the time step. Furthermore, a relatively coarse spatial discretization can be used (Secomb *et al.*, 2004), because the steep spatial gradients around each vessel are represented in the solution by the time-dependent Green’s function associated with each vessel source. While this approach is more complex to develop and implement than conventional methods for reaction–convection–diffusion systems, it permits efficient numerical simulations that would otherwise be computationally expensive or impractical.

To illustrate an application of this work, the method is used to analyse the kinetics of washout in the outflowing blood of an inert diffusible tracer substance from a region of tissue perfused by a heterogeneous network of microvessels. The analysis of tracer washout is relevant for experimental and clinical measurements of blood flow (Zierler, 1965), and provides a model for the washout of anaesthetic gases from tissue (Baker and Farmery, 2011). This problem is also of considerable theoretical interest as a prototype for more complex mass transport problems (Bassingthwaighe *et al.*, 1989; Beard and Bassingthwaighe, 2001). For simplified geometries, solutions can be obtained by other theoretical methods (Secomb, 2015), allowing direct comparisons with test the present method.

2. Methods

2.1 Governing equations in tissue

We consider the transport and reaction of N_s reacting solutes. The tissue is represented as a homogeneous medium through which solute p ($1 \leq p \leq N_s$) diffuses with uniform diffusivity D_p . Typically, this diffusivity is an effective value, taking into account the heterogeneous transport properties of cells and extracellular spaces (Tai and Chang, 1974; Stroevé, 1977; El-Kareh *et al.*, 1993). Fick's law of diffusion and the principle of conservation of mass lead to the governing equations in the extravascular tissue space:

$$\frac{\partial C_p^t}{\partial t} - D_p \nabla^2 C_p^t = R_p(C_1^t, C_2^t, \dots, C_{N_s}^t) \quad (1)$$

for $p = 1, 2, \dots, N_s$, where C_p^t is the tissue concentration of solute p and R_p is the rate of production (or uptake if negative) of solute p , including reactions with other solutes. Transport across cellular membranes by active processes can be simulated by including additional non-diffusible reactants to represent intracellular solutes, and representing the cellular transport properties as reaction terms in the governing equations.

2.2 Governing equations in vessels

The intravascular concentration of solute p , averaged over the vessel cross-section, is denoted by $C_p^v(s, t)$, where s is distance along the segment. Here and throughout, superscripts v , t and e denote values within a vessel, in tissue and in tissue adjacent to a vessel, respectively. The rate of convective transport of solute p along a vessel segment is QC_p^v , where Q is the volume flow rate, which may be time dependent. Conservation of mass implies that

$$A \frac{\partial C_p^v}{\partial t} + Q \frac{\partial C_p^v}{\partial s} = -q_p \quad (2)$$

where A is the cross-section area and $q_p(s, t)$ is the rate of diffusion of solute p from the vessel per unit length.

The extravascular concentration $C_p^e(s, t)$ is defined as the tissue concentration C_p^t evaluated at the vessel wall, averaged around the vessel circumference. This may differ from the intravascular concentration for several reasons: (i) The microvessel wall may have a finite permeability to the solute, leading to gradients across the wall. (ii) Radial diffusion within the blood may require significant solute gradients. (iii) The solute may have different solubility or binding characteristics in blood to those in tissue. In order to incorporate these effects, we first express the concentrations in blood and tissue in terms of

a single variable X_p that is uniform at thermodynamic equilibrium. For example, X_p may be the concentration in aqueous solution that would be at equilibrium with the blood or tissue, or the partial pressure of a soluble gas. The concentration in tissue can then be expressed as $C_p^t = \alpha_p X_p^t$, where X_p^t is the value of X_p in the tissue and α_p^t is the solubility or the partition coefficient. The intravascular concentration may be a linear or non-linear function $C_p^v = f_p(X_p^v)$. An example is the Hill equation for oxyhaemoglobin saturation. The efflux of solute p through the vessel wall per unit length is then

$$q_p = P_p [X_p^v - X_p^e] = P_p [f_p^{-1}(C_p^v) - C_p^e/\alpha_p^t] \quad (3)$$

where P_p is a coefficient that depends on the permeability of the vessel wall to the solute and on intravascular mass transport characteristics. The special case in which resistance to solute diffusion both within the vessel and through the wall is negligible can be represented by taking the limit $P_p \rightarrow \infty$.

2.3 Boundary conditions

In the initial development of the steady-state method (Hsu and Secomb, 1989), a finite cuboidal domain was considered, with zero flux conditions on the boundaries (Fig. 1(a)). However, this ‘pointwise no-flux’ approach can lead to artefacts, because each boundary plane is equivalent to a plane of mirror symmetry in the solution, and non-uniformities in vascular distribution, such as avascular regions near boundaries, are effectively magnified by these mirror planes. To circumvent this problem, we assumed instead that the region D containing the network of vessels and the associated tissue is embedded in the infinite-domain \mathbf{R}^3 (Secomb *et al.*, 2004) and pointwise conditions on flux on the boundary of D are not imposed. A further advantage of this approach is that D can be of arbitrary shape. In this ‘infinite-domain’ approach, the mass transport characteristics of the region D should be representative of the tissue as a whole. This would not be satisfied if the total exchange of solute between D and the surrounding tissue was not zero. Therefore, an additional constraint is imposed, namely that the total diffusive flux across the boundary of D is zero (Secomb *et al.*, 2004) (Fig. 1(b)).

For the time-dependent problem, this constraint is imposed at all times. Introduction of this constraint requires a free variable, and the solute concentration in the limit of large distance from the tissue region is treated as an unknown function of time $G_{0p}(t)$, referred to as the ‘ambient concentration’. Conservation of mass then implies that the infinite region outside D contains a spatially uniform source $\bar{\psi}_p(t)$ where $dG_{0p}/dt = \bar{\psi}_p(t)$. The condition of zero net flux on the boundary implies that the total amount of solute in the tissue within D has a rate of change equal to the total of the sources in the region. The problem to be solved is therefore formulated as follows:

$$\frac{\partial C_p^t}{\partial t} - D_p \nabla^2 C_p^t = \psi_p(\mathbf{x}, t) \text{ for } \mathbf{x} \in \mathbf{R}^3 \text{ and } \int_D \left(\frac{\partial C_p^t}{\partial t} - \psi_p(\mathbf{x}, t) \right) dV = 0 \quad (4)$$

Here $\psi_p(\mathbf{x}, t)$ represents the distribution of solute sources and sinks, including reactions in the tissue and exchange with vessels, with $\psi_p(\mathbf{x}, t) = \bar{\psi}_p(t)$ outside D .

2.4 Green’s function approach

The application of the Green’s function approach to steady-state oxygen transport has been described previously (Secomb *et al.*, 2004). The steady Green’s function G_p for solute p is defined (Kellogg, 1953)

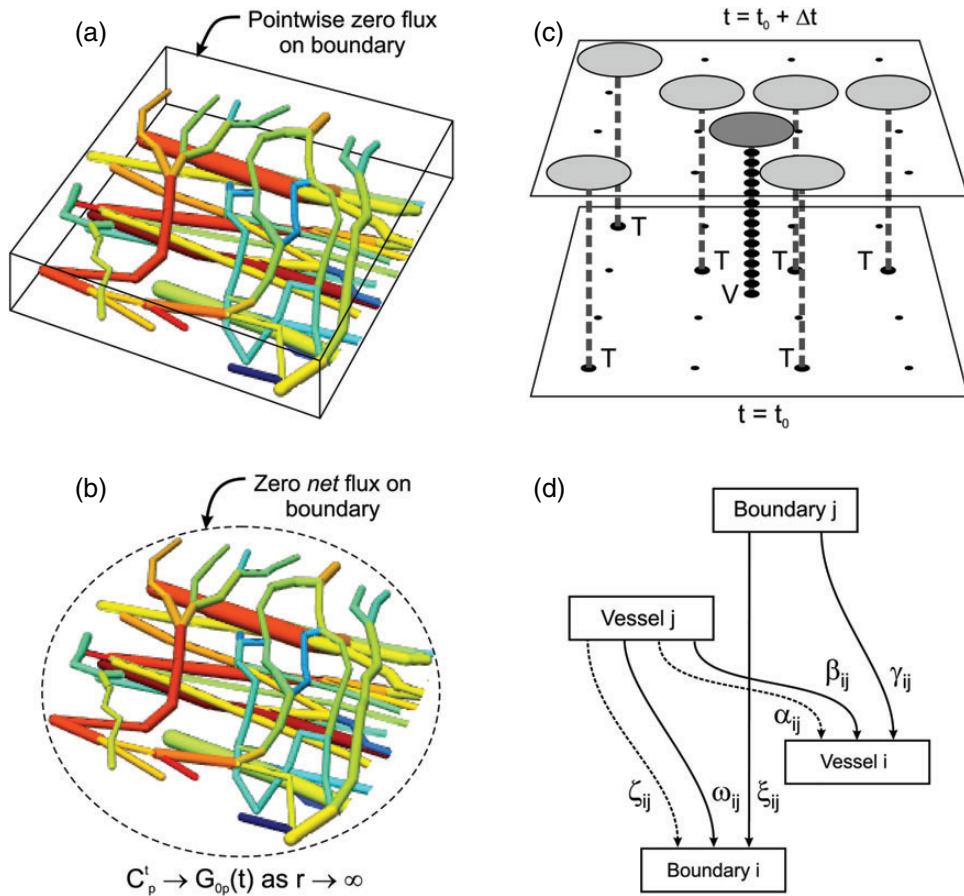


FIG. 1. Schematic illustrations of concepts underlying the computational method. (a) In the 'pointwise no-flux' approach, the condition of zero solute flux is applied on the boundary of a cuboidal box containing the vessel network. This approach leads to exaggerated boundary artefacts (see text) and is not used here. (b) In the 'infinite-domain' approach, the region D containing the network is considered to be embedded in an infinite domain, with zero net exchange of solute across the boundary of D . (c) Illustration of the time-dependent Green's function approach, for a 2D spatial domain. The lower plane represents a known distribution of solute level in the domain at time $t = t_0$, with tissue source points (large dots, T) and one vessel source point (V). At time $t = t_0 + \Delta t$ (upper plane), the solute that was at the tissue points is dispersed with a Gaussian dependence on distance from the source (light shaded discs), according to the Green's function defined in (9). A vessel point (V) provides a continuous source of solute (column of large dots) whose spread in the tissue is given by the integrated Green's function (17) (dark shaded disc). In practice, the diffusive spread during the interval Δt typically extends over multiple tissue points. (d) Matrices describing the convective redistribution of intravascular volume over one time step. The matrices β_{ij} , γ_{ij} , ξ_{ij} and ω_{ij} (solid curves) give the fraction of the blood contained in segment i or arriving at boundary node i that arrived from segment j or inflowing boundary node j during the time step. The matrices α_{ij} and ζ_{ij} (dashed curves) give the fraction of the time step that the blood contained in segment i or arriving at boundary node i spent in segment j , weighted according to the fraction of flow on each flow pathway.

as the concentration at a point \mathbf{x} resulting from a point source at \mathbf{x}^* , i.e. as the solution to

$$D_p \nabla^2 G_p = -\delta_3(\mathbf{x} - \mathbf{x}^*) \quad (5)$$

where δ_3 represents the 3D delta function. In the infinite-domain \mathbf{R}^3 , the solution that decays to zero at infinity is

$$G_p = \frac{1}{4\pi D_p |\mathbf{x} - \mathbf{x}^*|} \quad (6)$$

The tissue concentration field of solute p is represented as an integral over the domain

$$C_p(\mathbf{x}) = \int_D G_p(\mathbf{x} - \mathbf{x}^*) \psi_p(\mathbf{x}^*) d\mathbf{x}^* + G_0 \quad (7)$$

where $\psi_p(\mathbf{x})$ is an unknown function representing a distribution of solute sources and sinks lying within a domain $D \subset \mathbf{R}^3$, including contributions from vessels and tissue, and G_0 is an unknown constant.

For the time-dependent diffusion equation in unbounded 3D space, the unsteady Green's function $G_p(\mathbf{x} - \mathbf{x}^*, t - t^*)$ is the concentration at a point \mathbf{x} and time t resulting from an instantaneous source at point \mathbf{x}^* and time t^* , i.e. the solution to

$$\frac{\partial G_p}{\partial t} - D_p \nabla^2 G_p = \delta_3(\mathbf{x} - \mathbf{x}^*) \delta(t - t^*) \quad (8)$$

where δ denotes the Dirac delta function. The solution for $t > t^*$ that decays to zero at infinity is (Carslaw and Jaeger, 1959)

$$G_p(\mathbf{x} - \mathbf{x}^*, t - t^*) = (4\pi D_p(t - t^*))^{-3/2} \exp \left[-r^2 / (4D_p(t - t^*)) \right] \quad (9)$$

where $r = |\mathbf{x} - \mathbf{x}^*|$. The concentration of solute p is represented as an integral over space and time:

$$C_p(\mathbf{x}, t) = \int_0^t \int_{\mathbf{R}^3} G_p(\mathbf{x} - \mathbf{x}^*, t - t^*) \psi_p(\mathbf{x}^*, t^*) d\mathbf{x}^* dt^* + C_{0p} \quad (10)$$

where C_{0p} is an initial uniform concentration. The field at time t due to an instantaneous point source at time t^* as defined by (10) can also be computed by evaluating it at an intermediate time t' where $t^* < t' < t$ and then evaluating (10) a second time considering the resulting field as a source at time t' . Therefore, G_p has the following property, which may be verified by direct integration:

$$G_p(\mathbf{x} - \mathbf{x}^*, t - t^*) = \int_{\mathbf{R}^3} G_p(\mathbf{x} - \mathbf{x}', t - t') G_p(\mathbf{x}' - \mathbf{x}^*, t' - t^*) d\mathbf{x}' \quad (11)$$

This property provides the basis for the advancing the solution with time, as described below.

The integration in (10) can be restricted to a finite domain, by writing

$$\begin{aligned} C_p(\mathbf{x}, t) &= \int_0^t \int_{\mathbf{R}^3} G_p(\mathbf{x} - \mathbf{x}^*, t - t^*) [\psi_p(\mathbf{x}^*, t^*) - \bar{\psi}_p(t^*)] d\mathbf{x}^* dt^* \\ &\quad + \int_0^t \int_{\mathbf{R}^3} G_p(\mathbf{x} - \mathbf{x}^*, t - t^*) \bar{\psi}_p(t^*) d\mathbf{x}^* dt^* + C_{0p} \end{aligned} \quad (12)$$

By assumption, $\psi_p(\mathbf{x}^*, t^*) - \bar{\psi}_p(t^*) = 0$ for \mathbf{x}^* outside D . The second integral is independent of \mathbf{x} and reduces to the time integral of $\bar{\psi}_p(t)$. Therefore,

$$C_p(\mathbf{x}, t) = \int_0^t \int_D G_p(\mathbf{x} - \mathbf{x}^*, t - t^*) [\psi_p(\mathbf{x}^*, t^*) - \bar{\psi}_p(t^*)] d\mathbf{x}^* dt^* + G_{0p}(t) \quad (13)$$

where

$$\frac{dG_{0p}}{dt} = \bar{\psi}_p(t) \quad \text{and} \quad G_{0p}(0) = C_{0p} \quad (14)$$

It follows from (13) and the properties of G_p that $C_p(\mathbf{x}, t) \rightarrow G_{0p}(t)$ as $|\mathbf{x}| \rightarrow \infty$, confirming that $G_{0p}(t)$ is the ‘ambient’ concentration.

2.5 Numerical formulation: discretization in time

In the numerical procedure, the time interval $[0, t]$ is divided into n equal subintervals $[t_{k-1}, t_k]$ of length Δt , for $k = 1, \dots, n$ where $t_0 = 0$ and $t_n = t$, and $\psi_p(\mathbf{x}, t)$ is approximated by a time-independent function $\psi_{pk}(\mathbf{x})$ on subinterval $[t_{k-1}, t_k]$, with $\bar{\psi}_{pk}$ similarly defined. The contribution of a constant unit point source at \mathbf{x}^* during this time interval to the field at a later time t is:

$$\bar{G}_{pk}(\mathbf{x} - \mathbf{x}^*, t) = \int_{t_{k-1}}^{t_k} G_p(\mathbf{x} - \mathbf{x}^*, t - t^*) dt^* \quad (15)$$

This integral may be evaluated in terms of the error function (erf) as:

$$\bar{G}_{pk}(\mathbf{x} - \mathbf{x}^*, t) = (4\pi D_p r)^{-1} \left\{ \operatorname{erf} [r/(4D_p(t - t_k))^{1/2}] - \operatorname{erf} [r/(4D_p(t - t_{k-1}))^{1/2}] \right\} \quad (16)$$

where $r = |\mathbf{x} - \mathbf{x}^*|$. In particular, the field at the end of the time interval Δt resulting from a constant unit point source at \mathbf{x}^* over that interval is given by

$$\bar{G}_p(\mathbf{x} - \mathbf{x}^*, \Delta t) = (4\pi D_p r)^{-1} \left\{ 1 - \operatorname{erf} [r/(4D_p \Delta t)^{1/2}] \right\} \quad (17)$$

The steady result (6) is recovered as $\Delta t \rightarrow \infty$.

From the preceding results, it follows that the field at time $t = t_k$ (relative to the ambient concentration) can be obtained by convoluting the field at a preceding time $t = t_{k-1}$ with the Green's function for that interval, and adding the concentration resulting from the source distribution during the interval $[t_{k-1}, t_k]$:

$$\begin{aligned} C_p(\mathbf{x}, t_k) - G_{0pk} &= \int_D G_p(\mathbf{x} - \mathbf{x}^*, \Delta t) [C_p(\mathbf{x}^*, t_{k-1}) - G_{0pk-1}] d\mathbf{x}^* \\ &+ \int_D \bar{G}_p(\mathbf{x} - \mathbf{x}^*, \Delta t) [\psi_{pk}(\mathbf{x}^*) - \bar{\psi}_{pk}] d\mathbf{x}^* \end{aligned} \quad (18)$$

where from (14):

$$\bar{\psi}_{pk} = (G_{0pk} - G_{0pk-1})/\Delta t \quad (19)$$

and $G_{0pk} = G_{0p}(t_k)$. Equation (18) is obtained by expressing the right-hand side of (13) as the sum of integrals over $[0, t_{k-1}]$ and $[t_{k-1}, t_k]$, applying (11) to the first of these integrals (with $t = t_k$ and $t' = t_{k-1}$),

and applying (15) to the second integral. The first integral in (18) is approximated by its integral over the domain D , instead of \mathbf{R}^3 as in (11), because, as noted above, the field $C_p(\mathbf{x}, t) - G_{0p}(t)$ decays to zero outside D . The advantage of this formulation with regard to computation is that the field is calculated at each time point based on the field at the preceding time point, without the need to retain the complete history of the source strengths. Furthermore, the integrals have the form of convolutions, which are amenable to parallel processing.

2.6 Numerical formulation: discretization in space

The basic concept underlying the approach is illustrated schematically in Fig. 1(c). The network of vessels is divided into N_v short cylindrical segments. The tissue region, including vessels, is divided into N_t small cuboidal regions of volume V^t . Six diffusive interaction matrices are defined for each solute p , as follows. The matrices $G_{pij}^t (N_t \times N_t)$ and $G_{pij}^{vt} (N_v \times N_t)$ give the average concentration at $t = t_k$ in tissue region i and on the surface of segment i , respectively, resulting from a unit concentration of solute distributed over tissue region j at $t = t_{k-1}$. The matrices $\tilde{G}_{pij}^t (N_t \times N_t)$ and $\tilde{G}_{pij}^{vt} (N_v \times N_t)$ give the average concentration at $t = t_k$ in tissue region i and on the surface of segment i , respectively, resulting from a unit source distributed over tissue region j during the preceding interval Δt . The matrices $\tilde{G}_{pij}^{tv} (N_t \times N_v)$ and $\tilde{G}_{pij}^{vv} (N_v \times N_v)$ give the average concentration at $t = t_k$ in tissue region i and on the surface of segment i , respectively, resulting from a unit source distributed over the interior of segment j during the preceding interval Δt . This approach differs from the definition of the vessel sources as surface fluxes in (3). However, the resulting error is negligible compared with the error resulting from discretizing the vessel into segments with uniform source strength, provided that the segment lengths are much larger than their radii, which is typically the case. Details of the calculation of these matrices are given in Supplementary Material, S1.

The Green's function representation (18) is then expressed in a discrete form as:

$$C_{pik}^t = \sum_{j=1}^{N_t} V^t G_{pij}^t (C_{pik-1}^t - G_{0pk-1}) + \sum_{j=1}^{N_t} \tilde{G}_{pij}^t (\phi_{pjk} - V^t (G_{0pk} - G_{0pk-1}) / \Delta t) + \sum_{j=1}^{N_v} \tilde{G}_{pij}^{tv} q_{pjk} + G_{0pk} \quad \text{for } i = 1, \dots, N_t \quad (20)$$

$$C_{pik}^e = \sum_{j=1}^{N_t} V^t G_{pij}^{vt} (C_{pik-1}^t - G_{0pk-1}) + \sum_{j=1}^{N_t} \tilde{G}_{pij}^{vt} (\phi_{pjk} - V^t (G_{0pk} - G_{0pk-1}) / \Delta t) + \sum_{j=1}^{N_v} \tilde{G}_{pij}^{vv} q_{pjk} + G_{0pk} \quad \text{for } i = 1, \dots, N_v \quad (21)$$

for solute p and time step k . Here, C_{pik}^e is the average extravascular concentration of solute p over the surface of segment i , C_{pik}^t is the average concentration of solute p over tissue region i and G_{0pk} is an unknown constant. The quantities q_{pjk} and ϕ_{pjk} represent the unknown source strengths during time step k associated with the vessel segments and the tissue regions. This formulation leads to an implicit numerical scheme that is stable and well behaved even if the time step is not small.

The tissue source strengths φ_{pjk} during each time step k are computed using the specified reaction rates R_p evaluated for the average of the tissue solute levels at the beginning and end of the time step:

$$\phi_{pjk} = V^t R_p (\bar{C}_{1jk}^t, \bar{C}_{2jk}^t, \dots, \bar{C}_{N_{ijk}-1}^t) \quad \text{for } j = 1, \dots, N_t \quad (22)$$

where $\bar{C}_{ijk}^t = (C_{ijk-1}^t + C_{ijk}^t)/2$.

By integrating (2) along each flow pathway in the network, the concentration of solute p in vessel segment i at a time $t = t_k$ can be expressed as a linear function of the corresponding concentrations at the preceding time point $t = t_{k-1}$ and of the source strengths q_{pjk} :

$$C_{pik}^v = \sum_{\substack{j=1 \\ \text{inflow}}}^{N_b} \gamma_{ij} C_{pjk}^b + \sum_{j=1}^{N_v} \beta_{ij} C_{pjk-1}^v - \sum_{j=1}^{N_v} \alpha_{ij} q_{pjk} \Delta t / V_j \quad \text{for } i = 1, \dots, N_v \quad (23)$$

where V_j is the volume of segment j . The matrix γ_{ij} gives the fraction of the blood contained in segment i at time $t = t_k$ that arrived from inflowing boundary node j during time step k , C_{pjk}^b is the (prescribed) concentration of solute p in the inflowing blood at boundary node j during time step k and N_b is the number of boundary nodes. The matrix β_{ij} gives the fraction of the blood contained in segment i at time $t = t_k$ that arrived from segment j during time step k . The matrix α_{ij} gives the fraction of the time step Δt that the blood contained in segment i at time $t = t_k$ spent in segment j , weighted according to the fraction of flow on each flow pathway. In order to compute the washout of solutes in the outflowing blood, the following relationship is used:

$$C_{pik}^b = \sum_{\substack{j=1 \\ \text{inflow}}}^{N_b} \xi_{ij} C_{pjk}^b + \sum_{j=1}^{N_v} \omega_{ij} C_{pjk-1}^v - \sum_{j=1}^{N_v} \zeta_{ij} q_{pjk} \Delta t / V_j \quad \text{for } i = 1, \dots, N_b \text{ (outflow nodes)} \quad (24)$$

where C_{pik}^b is the average concentration of solute p in the outflowing blood at boundary node i during time step k , ξ_{ij} and ω_{ij} give the fractions of the outflowing blood that arrived from boundary node j and from segment j , respectively, and ζ_{ij} gives the fraction of the time step that the outflowing blood spent in segment j , weighted as for α_{ij} . This equation differs from (23) in that it refers to the blood arriving at a boundary node during a time step, whereas (23) refers to the contents of a segment at the end of the time step.

The dimensionless convective matrices α_{ij} , β_{ij} , γ_{ij} , ξ_{ij} , ω_{ij} and ζ_{ij} depend on the distribution of flow velocities in the network, and are computed as described in Supplementary Material, S1. The significance of these matrices with regard to the redistribution of intravascular volume over one time step is illustrated in Fig. 1(d). In the present implementation, blood is assumed to move in each segment with a single velocity Q/A . However, other effects such as the increased velocity of red blood cells (Fåhræus effect) or Taylor dispersion can be incorporated within this framework. While the computation of the above matrices is intricate, their availability is critical to success of the method, since it allows the use of computational time steps Δt that are arbitrarily large compared with the transit time of blood through individual vessel segments.

Equation (2), which relates the vessel source strengths to the intravascular and extravascular solute levels, gives in discrete form

$$q_{pik} = l_i P_{pi} [f_p^{-1} (C_{pik}^v) - C_{pik}^e / \alpha_p^t] \quad (25)$$

where l_i is the length of segment i . This may be combined with (21) and (23) to give

$$\begin{aligned} & \sum_{j=1}^{N_t} V^t G_{pij}^{vt} (C_{pik-1}^t - G_{0pk-1}) + \sum_{j=1}^{N_v} \bar{G}_{pij}^{vv} q_{pj k} + \sum_{j=1}^{N_t} \bar{G}_{pij}^{vt} (\phi_{pj k} - V^t (G_{0pk} - G_{0pk-1}) / \Delta t) + G_{0pk} \\ &= \alpha_p^t f_p^{-1} \left(\sum_{j=1}^{N_b} \gamma_{ij} C_{pj k}^b + \sum_{j=1}^{N_v} \beta_{ij} C_{pj k-1}^v - \sum_{j=1}^{N_v} \alpha_{ij} q_{pj k} \Delta t / V_j \right) - \alpha_p^t q_{pik} / (l_i P_{pi}) \quad \text{for } i = 1, \dots, N_v \end{aligned} \quad (26)$$

Here, the left-hand side gives the average tissue concentration adjacent to segment i based on tissue transport, whereas the right-hand side gives the same quantity based on vessel transport.

Condition (4) of zero net diffusive exchange at the boundaries of D gives

$$\sum_{j=1}^{N_t} \phi_{pj k} + \sum_{j=1}^{N_v} q_{pj k} = (V^t / \Delta t) \sum_{i=1}^{N_t} (C_{pik}^t - C_{pik-1}^t) \quad (27)$$

where C_{pik}^t is given by (20). Source strengths during the interval are expressed as the average of their initial and final values, consistent with the implicit numerical scheme.

The solution procedure at time step k is as follows. (i) The tissue source strengths $\phi_{pj k}$ are computed using (22). (ii) Initial estimates of the vessel source strengths $q_{pj k}$ are chosen, typically by setting $q_{pj k} = q_{pj k-1}$. (iii) The function f_p^{-1} in (26) is linearized about the current values of its arguments (see Supplementary Material, S1). Equations (26) and (27) then comprise a linear system of $N_v + 1$ equations for the variables $q_{pj k}$ ($j = 1, \dots, N_v$) and G_{0pk} , which is solved using the biconjugate gradient stabilized method. (iv) The updated values of $C_{pj k}^t$ are computed using (20). This computation is repeated iteratively using updated values of $q_{pj k}$ until convergence is achieved.

At each time step, the tissue field is computed on a selected plane intersecting the tissue region and a contour plot is constructed to illustrate the behaviour. Solute levels are computed using (20), with matrices G_{pij}^{tt} , \bar{G}_{pij}^{tt} and \bar{G}_{pij}^{tv} as already described, except that subscript j here denotes a point in the selected plane.

2.7 Computational implementation

The algorithm is implemented in C++ on a personal computer. The code is available at <http://physiology.arizona.edu/people/secomb/greens>. A parallelized version is also implemented using a Tesla C1060 graphical processing unit (GPU) and the compute unified device architecture (CUDA) parallel computing platform and programming model (Nvidia Corporation, Santa Clara, CA, USA). In this version, the matrix operations required for the biconjugate gradient stabilized method are programmed using the cuBLAS library (Nvidia) and the numerical convolutions in (25) are evaluated using a custom CUDA kernel.

2.8 Definition of the washout problem

The application of the method is illustrated by simulating the washout of an inert diffusible solute from a region of tissue perfused by a microvascular network with a realistic inhomogeneous geometry. For purposes of comparison and testing, simulations are also carried out for a cylindrical tissue region

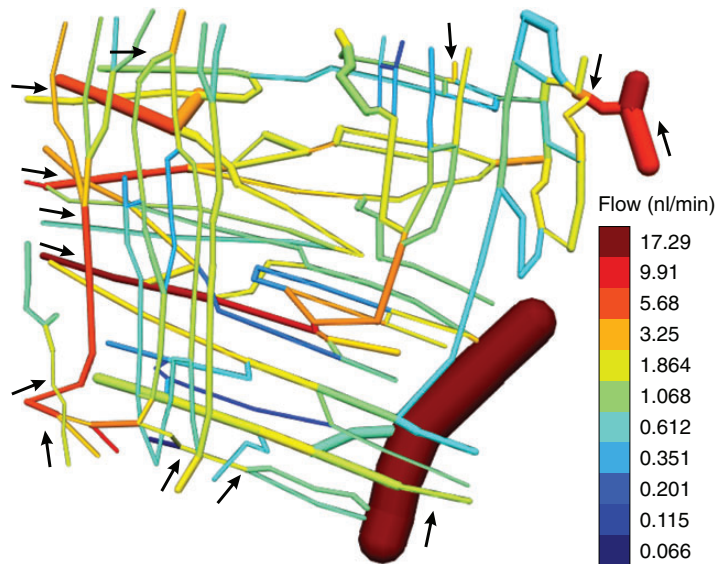


FIG. 2. Computer visualization of 3D microvessel network from rat cremaster muscle. Vessels shaded according to blood flow rate as shown at right. Arrows identify vessels feeding the network.

perfused by a single capillary. The solute is initially ($t = 0$) assumed to be distributed uniformly in the tissue. The concentration of solute in the blood in the vessel(s) at $t = 0$ and subsequently entering the vessel(s) is assumed to be zero. The flow-weighted average concentration in the vessel(s) exiting the region is computed as a function of time. Effects of varying solute diffusivity D in the range $5\text{--}1000\ \mu\text{m}^2\ \text{s}^{-1}$ and permeability P in the range $1\text{--}10\ \mu\text{m}\ \text{s}^{-1}$ are examined. Computations are carried out with time steps Δt ranging from 0.25 to 100 s.

2.9 Vascular geometries

Data on vascular network geometry and blood flow distribution used in the simulations are based on previous observations of a microvessel network in the rat cremaster muscle (Secomb *et al.*, 2004). In that study, blood flow rates were estimated using intravital microscopy by counting the passage of fluorescently labelled red blood cells along 62 distinct flow pathways through the network. The 3D vascular geometry was reconstructed based on observations of fluorescently labelled vessel walls by confocal microscopy (Fig. 2). The network contains 295 segments with a total length of 20.395 mm. In the numerical simulations, segments longer than $100\ \mu\text{m}$ are subdivided, and the number of vessel points is $N_v = 350$. The vascular network has overall dimensions of $1.1 \times 1.0 \times 0.24\ \text{mm}$. A rectangular grid of points is set up with a spacing of $15\ \mu\text{m}$ and the tissue region included in the simulation is defined by those grid points that lie within the convex hull of the network, i.e. the minimal convex region containing the network. This irregularly shaped region has a volume of 63.81 nl, and contains $N_t = 18,916$ tissue points. The overall microvessel length density is $319.6\ \text{mm}^{-2}$. The total blood flow rate to the network is 74.97 nl/min, and the blood perfusion (flow rate divided by tissue volume) is $1.1748\ \text{min}^{-1}$.

To examine the effect of heterogeneous network structure on solute washout, the results are compared with those for a corresponding Krogh cylinder geometry. Originally developed to describe oxygen

transport in skeletal muscle (Krogh, 1919), the Krogh model assumes a homogeneous vascular geometry consisting of an array of identical straight, uniformly spaced capillaries, each of which exchanges solute only with a surrounding cylindrical tissue region. To allow a direct comparison with the cremaster network, the geometrical parameters of the Krogh model are chosen to give the same vessel length per tissue volume and vessel surface area per tissue volume. The capillary radius is then $r_c = 5.767 \mu\text{m}$ and the tissue radius is $r_t = 31.56 \mu\text{m}$. The cremaster network contains multiple flow pathways with varying lengths. The length L of the Krogh cylinder is defined by taking the flow-weighted mean of all the pathway lengths in the network (Secomb *et al.*, 2000), giving $L = 634.9 \mu\text{m}$. The flow velocity in the capillary is $u_0 = 372.3 \mu\text{m/s}$, for a flow rate of 1.987 nl/min and perfusion $p = 1.1748 \text{ min}^{-1}$, equal to that in the cremaster network.

3. Results

3.1 Solute washout from the cremaster network

Simulations were performed for a microvessel network in the rat cremaster muscle, as shown in Fig. 2, for which data on vascular network geometry and blood flow distribution were obtained previously (Secomb *et al.*, 2004). In the simulations, the solute concentration is initially set to a uniform level in the tissue, the concentration in the inflowing blood is set to zero and the spatial distribution of solute concentration is computed as a function of time. Figure 3 illustrates the solute distribution in the vessels and in the tissue after 30 s, for various values of tissue diffusivity D and vessel wall permeability P . When both parameters are relatively high (Fig. 3(a): $D = 500 \mu\text{m}^2 \text{ s}^{-1}$ and $P = 10 \mu\text{m s}^{-1}$), tissue gradients are shallow and the concentration in the outflowing blood is almost equilibrated with the surrounding tissue. About 42% of the solute is washed out within 30 s. With a 10-fold reduction in diffusivity (Fig. 3(b): $D = 50 \mu\text{m}^2 \text{ s}^{-1}$ and $P = 10 \mu\text{m s}^{-1}$), tissue concentration gradients are steeper and vessel concentrations do not equilibrate with tissue, resulting in slower washout, with about 33% washed out within 30 s. If the vessel permeability is also reduced 10-fold (Fig. 3(c): $D = 50 \mu\text{m}^2 \text{ s}^{-1}$ and $P = 1 \mu\text{m s}^{-1}$), tissue gradients are reduced, the tissue concentration is much lower than the intravascular concentration, and washout is about 17% after 30 s. It is also evident that the difference between vessel and tissue concentrations is reduced in slow-flowing vessels, as, for example, in the narrow vessel that flows from lower to upper right in Fig. 3. These results are consistent with well-known concepts of mass transport. A typical simulation with parameters as in Fig. 3(a) and 50 1-s time steps took about 60 min on a laptop computer and 4.5 min using parallel processing with a GPU.

In this method, the network of vessels is considered to be embedded in an infinite space and the ambient solute concentration far from the network is an unknown function of time. The solute concentration in the outflowing blood and the ambient concentration are shown in Fig. 4 as functions of time for the same three cases as in Fig. 3. For the network, the outflow concentration is calculated as the flow-weighted average of the concentrations in all outflowing segments. After an initial transient, both concentrations decline exponentially at the same rate. Although it might be expected that a heterogeneous network structure would lead to a multi-exponential washout curve (Beard and Bassingthwaite, 1998), such behaviour is not found in the present simulations (see Discussion).

3.2 Comparison with washout from the corresponding Krogh cylinder geometry

For each case considered, the rate constant λ of the exponential decay of outflow concentration is evaluated. Figure 5 shows predicted values of the ratio λ/p , where p is the perfusion (blood flow rate divided by tissue volume). Results are also shown for the corresponding

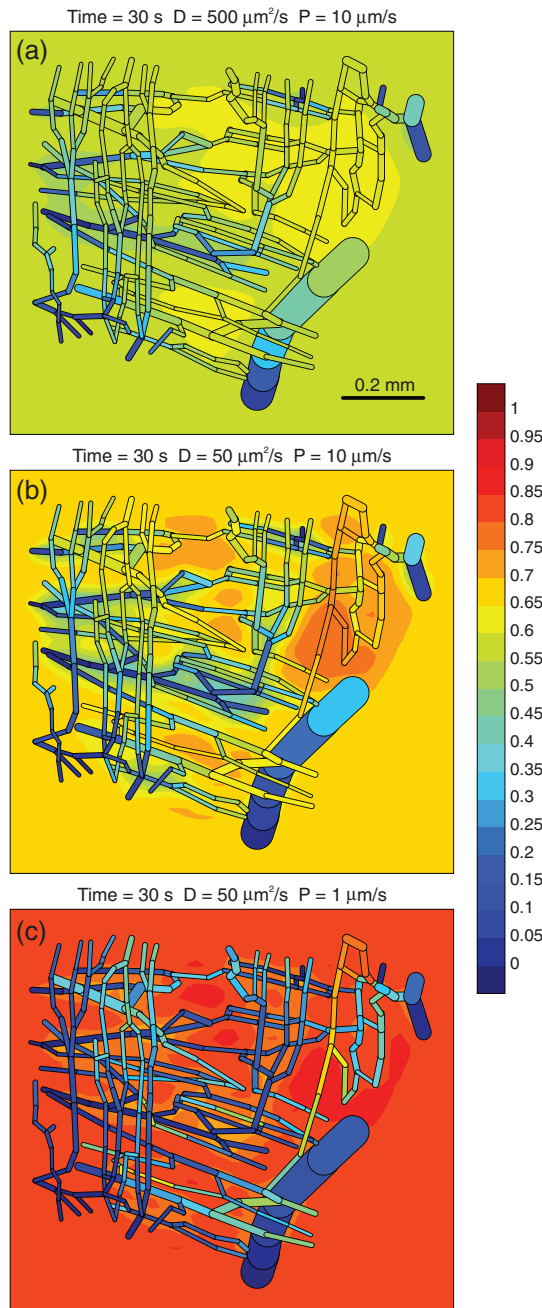


FIG. 3. Simulated solute distributions after 30 s of washout. Tissue surrounding a network in the rat cremaster muscle is initially loaded with a unit concentration of solute. The bar at right gives solute concentrations. Vessels are shown projected onto a plane lying approximately in the middle of the network region. Tissue levels in the plane are also shown. Time step in simulations $\Delta t = 1$ s. Values of tissue diffusivity D and vessel wall permeability P : (a) $D = 500 \mu\text{m}^2 \text{s}^{-1}$, $P = 10 \mu\text{m} \text{s}^{-1}$, (b) $D = 50 \mu\text{m}^2 \text{s}^{-1}$, $P = 10 \mu\text{m} \text{s}^{-1}$, (c) $D = 50 \mu\text{m}^2 \text{s}^{-1}$, $P = 1 \mu\text{m} \text{s}^{-1}$. See Supplementary Material S2 for corresponding movie files.

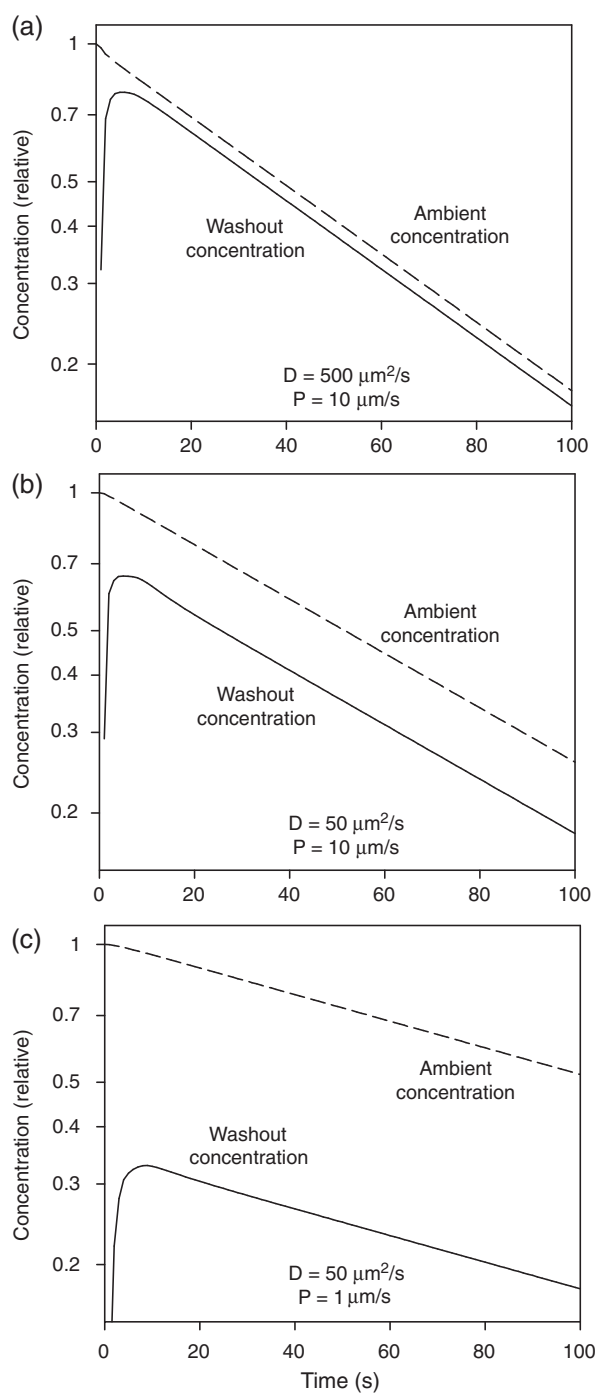


FIG. 4. Variation with time of outflowing and ambient solute concentrations (logarithmic scale) during simulated washout. Both concentrations decline exponentially with time. Values of tissue diffusivity D and vessel wall permeability P are as in Fig. 3.

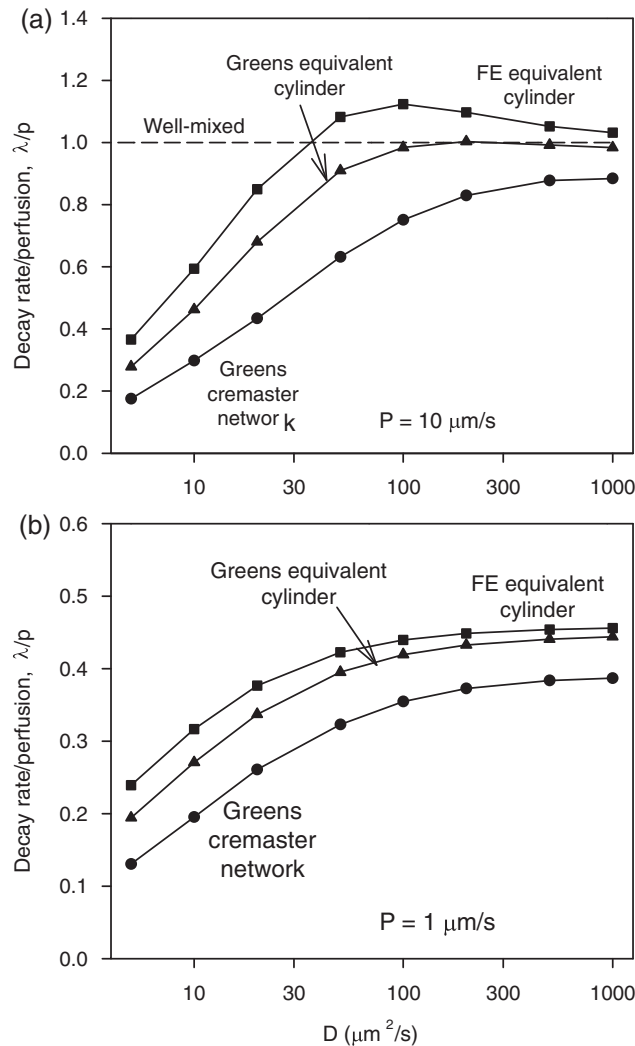


FIG. 5. Ratio of solute concentration decay rate to perfusion (λ/p), as a function of solute diffusivity D . Results are shown for three cases: Green's function method for the cremaster network, and Green's function and FE methods for the equivalent cylinder model. Time step Δt varies with D , such that $D\Delta t = 500 \mu\text{m}^2$. Permeability values: (a) $P = 10 \mu\text{m/s}$, (b) $P = 1 \mu\text{m/s}$. The reductions in decay rates for the network relative to the equivalent cylinder model show the effects of heterogeneous network structure.

Krogh cylinder geometry as defined above, for which two computational approaches are used, the Green's function method and the infinite-domain finite-element (FE) method developed previously (Secomb, 2015).

We consider first the results obtained for the equivalent cylinder geometry using the Green's function method. When diffusivity and permeability are relatively high (e.g. $D = 500 \mu\text{m}^2 \text{s}^{-1}$ and $P = 10 \mu\text{m/s}$), the washout is perfusion-limited and the ratio λ/p is close to unity (Fig. 5(a)). The condition $\lambda/p = 1$ would apply if the tissue space acted as a well-mixed compartment with a solute concentration

equal to that in the outflowing blood. With decreasing diffusivity, diffusion becomes limiting and λ/p declines. When the vessel permeability is reduced to $P = 1 \mu\text{m s}^{-1}$, λ/p is further reduced (Fig. 5(b)).

Calculations were also performed for the equivalent cylinder geometry using the previously described ‘infinite-domain’ FE method (Secomb, 2015). Predicted washout rates show similar trends but are slightly higher than those obtained by the Green’s function method. The difference is largest for intermediate values of D when $P = 10 \mu\text{m s}^{-1}$. The discrepancy between the methods is a result of the different assumed boundary conditions. In both methods, the cylindrical tissue region is assumed to be embedded in a much larger outer region, with which it can exchange solute. Values of λ/p greater than 1 occur when a standing axial gradient of concentration is set up in the tissue region, with higher concentrations near the downstream end of the vessel. In the infinite-domain FE method, these gradients are partially inhibited by the effects of axial diffusion in the cylindrical ‘outer’ region surrounding the tissue cylinder (Secomb, 2015). In the Green’s function method, the concentration outside the tissue domain approaches a unique ambient concentration. This condition, which may be more realistic because the ‘outer’ region then has no artificial boundaries, has the effect of more strongly inhibiting the axial concentration gradient.

With regard to the cremaster network, the results show that the heterogeneity of the network structure results in slower washout than for the equivalent cylinder geometry, which represents a homogeneous network structure. The difference in predicted washout rates is in the range of approximately 10–30%. In the heterogeneous network, the distribution of distances from tissue points to the nearest vessel is shifted to larger distances, and the presence of low flow vessels that rapidly equilibrate with tissue solute levels effectively reduces the vessel area available for exchange. These two factors account for the reduction in washout rate in the cremaster network relative to a corresponding homogeneous structure.

3.3 Effect of varying time step

The effect on predicted washout rate of varying the time step Δt in the range 0.25–100 s is shown in Fig. 6 for several cases. The results are presented as functions of Δt and of the dimensionless quantity $D\Delta t/(\Delta x)^2$. Approximately consistent results are obtained for wide ranges of time steps. The decrease in computed λ/p values obtained with large time steps arises because the time step (up to 100 s) approaches the time constant of the exponential decay of the washout, which is from 60 to 150 s in these three cases. When $D = 50 \mu\text{m}^2 \text{s}^{-1}$ and $P = 10 \mu\text{m s}^{-1}$, an increase in computed λ/p values is found when small time steps are used. In this case, the actual diffusive spread of solute during each time step is small, and is artificially increased in the simulation due to the averaging of solute concentrations over finite tissue regions. The results in Fig. 6(b) imply that the method is not restricted to values of $D\Delta t/(\Delta x)^2$ less than 1. In particular, Fig. 5 results are for $D\Delta t/(\Delta x)^2 = 2.22$.

4. Discussion

Temporally and spatially resolved numerical simulations of phenomena involving convection and diffusion in a complex 3D geometry present considerable computational challenges. When finite-difference methods are used, the representation of both convective and diffusive processes leads to stringent limits on the time step Δt that can be used for a given distance step Δx . For geometries with fine structures that must be resolved, the distance step must be small, so that very small time steps are needed. The use of implicit schemes allows slightly larger time steps, at the expense of solving very large linear systems.

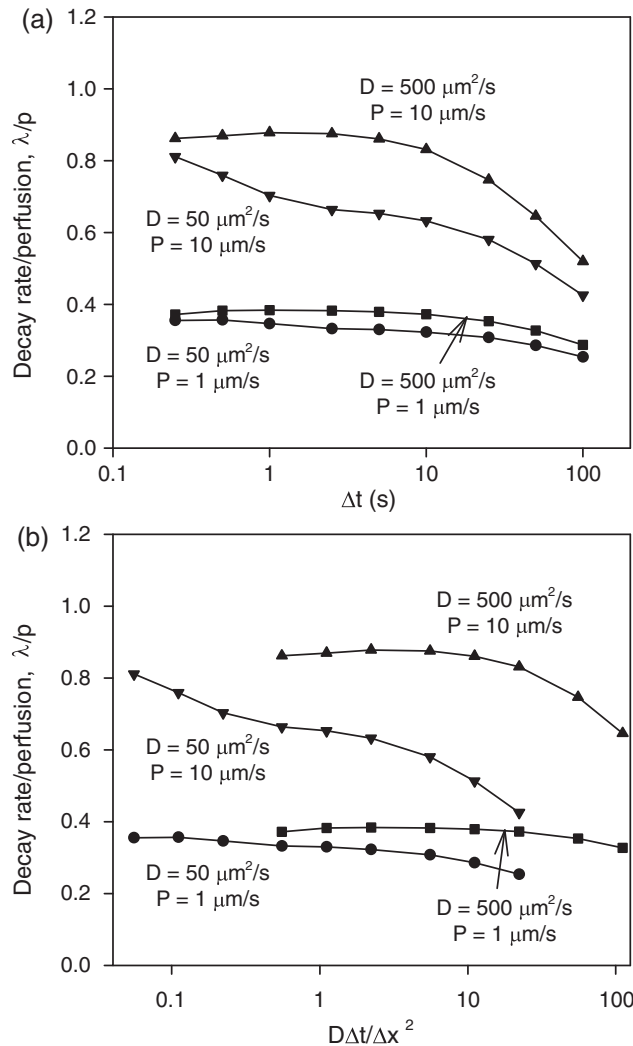


FIG. 6. Effect of varying the time step on the predicted values of λ/p . Values of tissue diffusivity D and vessel wall permeability P are indicated. (a) Results as functions of the time step Δt . (b) Results as functions of the dimensionless quantity $D\Delta t/(\Delta x)^2$.

The present method is designed to avoid these limitations, such that much larger time steps can be used. Two key features allow this. Firstly, at each time step, the effect of diffusion is represented by convoluting the concentration field at the beginning of a time step with the Green's function for the time-dependent diffusion equation. This allows diffusive propagation of solute concentration over multiple spatial grid points in a single time step. Secondly, the convective transport of solute within the vascular network is represented by a set of matrices that can be computed for an arbitrarily large time step, so that convective solute transport over any distance in a single time step is properly represented. The maximum time step that can be used is limited only by the time scales of the processes that are being simulated, and not by numerical criteria.

As an example of the application of the method, results are presented for the ‘washout’ problem, one of the most basic time-dependent problems of time-dependent mass transport in microvascular networks. The simulations are based on a previously studied network in the rat cremaster muscle, containing 295 vessel segments. The computational speed of the method is demonstrated by the fact that each simulation took a few minutes on a personal computer with a GPU. The washout concentration is found to decay exponentially with time after a brief initial transient. The predicted decay rate for the network structure observed in the rat cremaster is somewhat lower, by about 10–30%, than the decay rate for a tissue cylinder model representing a corresponding homogeneous structure.

In the cases considered here, the washout concentration quickly approaches a single decaying exponential function of time. This contrasts with the observation of power-law decay of the washout curve in experimental studies of coronary circulation, which can be explained as resulting from the weighted sum of a large number of exponentials with varying coefficients in the exponent (Beard and Bassingthwaite, 1998). In the present simulations, the diffusive coupling between points in the tissue region is strong enough that the entire tissue region is entrained to a single decay rate. The assumption that the tissue concentration approaches a single time-dependent ‘ambient’ concentration outside the network contributes to this coupling. The prediction of non-exponential decay of the washout curve would require the simulation of larger tissue regions, such that some subregions are not coupled diffusively.

The results presented here are for a single inert solute, with linear solubility. The method is also applicable to the case of multiple reacting solutes, with linear or non-linear reaction kinetics and linear or non-linear binding characteristics in blood. These non-linearities are handled by the use of an iterative scheme to solve (26) and (27), as described in detail in the Supplementary Material. As indicated by (22), the reaction rates are calculated using updated solute concentrations, resulting in an implicit time-stepping scheme. This improves the stability of the system and allows larger time steps to be used, relative to an explicit scheme. Cases in which some of the solutes are non-diffusible can also be simulated, for example, to represent the exchange of a solute between extracellular and intracellular compartments. Examples of such applications will be presented elsewhere.

In summary, the novel time-dependent Green’s function method described here provides an efficient computational tool for analysing time-dependent diffusion, convection and reaction in systems with complex geometries, with potential applications to a wide range of biological systems. Such applications arise naturally in the multi-scale modelling of biological systems (Walpole *et al.*, 2013) and in studies addressing the goals of the Physiome project (Hunter, 2004). For example, in the development of cancer chemotherapies, transport characteristics influence the ability of drugs to penetrate all parts of a tumour (Beard, 2006; Baish *et al.*, 2011). Consideration of time-dependent transport properties may be helpful in understanding and predicting the cytotoxic effects of drugs, and in optimizing treatment schedules. As another example, spatially averaged compartmental models have so far been used in simulations of metabolic dynamics of tissues such as skeletal or cardiac muscle (Dash *et al.*, 2008; Bassingthwaite *et al.*, 2012). The approach developed here opens the possibility of analysing dynamic metabolic processes involving multiple reacting solutes, using spatially resolved models to represent gradients associated with the structure of the vasculature.

Supplementary material

Supplementary material is available at <http://imammb.oxfordjournals.org>.

Funding

This work was supported by NIH Grants CA040355, HL034555 and HL070657.

REFERENCES

- BAISH, J. W., STYLIANOPOULOS, T., LANNING, R. M., KAMOUN, W. S., FUKUMURA, D., MUNN, L. L. & JAIN, R. K. (2011) Scaling rules for diffusive drug delivery in tumor and normal tissues. *Proc. Natl Acad. Sci. USA*, **108**, 1799–1803.
- BAKER, A. B. & FARMERY, A. D. (2011) Inert gas transport in blood and tissues. *Compr. Physiol.*, **1**, 569–592.
- BASSINGTHWAIGHTE, J. B., BEARD, D. A., CARLSON, B. E., DASH, R. K. & VINNAKOTA, K. (2012) Modeling to link regional myocardial work, metabolism and blood flows. *Ann. Biomed. Eng.*, **40**, 2379–2398.
- BASSINGTHWAIGHTE, J. B., WANG, C. Y. & CHAN, I. S. (1989) Blood-tissue exchange via transport and transformation by capillary endothelial cells. *Circ. Res.*, **65**, 997–1020.
- BEARD, D. A. (2006) Modeling of oxygen transport and cellular energetics explains observations on in vivo cardiac energy metabolism. *PLoS Comput. Biol.*, **2**, e107.
- BEARD, D. A. & BASSINGTHWAIGHTE, J. B. (1998) Power-law kinetics of tracer washout from physiological systems. *Ann. Biomed. Eng.*, **26**, 775–779.
- BEARD, D. A. & BASSINGTHWAIGHTE, J. B. (2001) Modeling advection and diffusion of oxygen in complex vascular networks. *Ann. Biomed. Eng.*, **29**, 298–310.
- BEARD, D. A., SCHENKMAN, K. A. & FEIGL, E. O. (2003) Myocardial oxygenation in isolated hearts predicted by an anatomically realistic microvascular transport model. *Am. J. Physiol Heart Circ. Physiol.*, **285**, H1826–H1836.
- CARSLAW, H. S. & JAEGER, J. C. (1959) *Conduction of Heat in Solids*. 2nd edn. Oxford: Oxford University Press.
- DASH, R. K., LI, Y., KIM, J., BEARD, D. A., SAIDEL, G. M. & CABRERA, M. E. (2008) Metabolic dynamics in skeletal muscle during acute reduction in blood flow and oxygen supply to mitochondria: in-silico studies using a multi-scale, top-down integrated model. *PLoS One*, **3**, e3168.
- EL-KAREH, A. W., BRAUNSTEIN, S. L. & SECOMB, T. W. (1993) Effect of cell arrangement and interstitial volume fraction on the diffusivity of monoclonal antibodies in tissue. *Biophys. J.*, **64**, 1638–1646.
- GOLDMAN, D. & POPEL, A. S. (2000) A computational study of the effect of capillary network anastomoses and tortuosity on oxygen transport. *J. Theor. Biol.*, **206**, 181–194.
- GOLDMAN, D. & POPEL, A. S. (2001) A computational study of the effect of vasomotion on oxygen transport from capillary networks. *J. Theor. Biol.*, **209**, 189–199.
- GROEBE, K. (1990) A versatile model of steady state O₂ supply to tissue. *Application to skeletal muscle*. *Biophys. J.*, **57**, 485–498.
- HICKS, K. O., PRUIJN, F. B., SECOMB, T. W., HAY, M. P., HSU, R., BROWN, J. M., DENNY, W. A., DEWHIRST, M. W. & WILSON, W. R. (2006) Use of three-dimensional tissue cultures to model extravascular transport and predict in vivo activity of hypoxia-targeted anticancer drugs. *J. Natl Cancer Inst.*, **98**, 1118–1128.
- HOOFD, L. (1992) Updating the Krogh model—assumptions and extensions. *Oxygen Transport in Biological Systems: Modelling of Pathways from Environment to Cell* (S. Egginton and H. F. Ross eds). Cambridge: Cambridge University Press, pp. 197–229.
- HOOFD, L., OLDERS, J. & TUREK, Z. (1990) Oxygen pressures calculated in a tissue volume with parallel capillaries. *Adv. Exp. Med. Biol.*, **277**, 21–29.
- HSU, R. & SECOMB, T. W. (1989) A Green's function method for analysis of oxygen delivery to tissue by microvascular networks. *Math. Biosci.*, **96**, 61–78.
- HUNTER, P. J. (2004) The IUPS Physiome Project: a framework for computational physiology. *Prog. Biophys. Mol. Biol.*, **85**, 551–569.
- JAIN, R. K. (2005) Normalization of tumor vasculature: an emerging concept in antiangiogenic therapy. *Science*, **307**, 58–62.
- KELLOGG, O. D. (1953) *Foundations of Potential Theory*. New York: Dover.

- KROGH, A. (1919) The number and the distribution of capillaries in muscle with the calculation of the oxygen pressure necessary for supplying the tissue. *J. Physiol. (Lond)*, **52**, 409–515.
- LO, A., FUGLEVAND, A. J. & SECOMB, T. W. (2003) Oxygen delivery to skeletal muscle fibers: effects of microvascular unit structure and control mechanisms. *Am. J. Physiol. Heart Circ. Physiol.*, **285**, H955–H963.
- MIDDLEMAN, S. (1972) *Transport Phenomena in the Cardiovascular System*. New York: John Wiley and Sons.
- PEPEL, A. S. (1989) Theory of oxygen transport to tissue. *Crit. Rev. Biomed. Eng.*, **17**, 257–321.
- SECOMB, T. W. (2015) Krogh-cylinder and infinite-domain models for washout of an inert diffusible solute from tissue. *Microcirculation*, **22**, 91–98.
- SECOMB, T. W. & HSU, R. (1988) Analysis of oxygen delivery to tissue by microvascular networks. *Adv. Exp. Med. Biol.*, **222**, 95–103.
- SECOMB, T. W., HSU, R., BEAMER, N. B. & COULL, B. M. (2000) Theoretical simulation of oxygen transport to brain by networks of microvessels: effects of oxygen supply and demand on tissue hypoxia. *Microcirculation*, **7**, 237–247.
- SECOMB, T. W., HSU, R., DEWHIRST, M. W., KLITZMAN, B. & GROSS, J. F. (1993) Analysis of oxygen transport to tumor tissue by microvascular networks. *Int. J. Radiat. Oncol. Biol. Phys.*, **25**, 481–489.
- SECOMB, T. W., HSU, R., PARK, E. Y. & DEWHIRST, M. W. (2004) Green's function methods for analysis of oxygen delivery to tissue by microvascular networks. *Ann. Biomed. Eng.*, **32**, 1519–1529.
- STROEVE, P. (1977) Diffusion with irreversible chemical-reaction in heterogeneous media—application to oxygen-transport in respiring tissue. *J. Theoret. Biol.*, **64**, 237–251.
- TAI, R. C. & CHANG, H. K. (1974) Oxygen transport in heterogeneous tissue. *J. Theor. Biol.*, **43**, 265–276.
- WALPOLE, J., PAPIN, J. A. & PEIRCE, S. M. (2013) Multiscale computational models of complex biological systems. *Annu. Rev. Biomed. Eng.*, **15**, 137–154.
- ZIERLER, K. L. (1965) Equations for measuring blood flow by external monitoring of radioisotopes. *Circ. Res.*, **16**, 309–321.